Green Chemistry

PAPER

View Article Online
View Journal | View Issue

Cite this: *Green Chem.*, 2023, **25**, 7318

Metal-free photocatalytic transformation of waste polystyrene into valuable chemicals: advancing sustainability through circular economy†

Rajat Ghalta,[a] Rajaram Bal[b] and Rajendra Srivastava*[a]

The present study offers a metal-free photocatalytic visible-light-driven protocol for addressing the plastic waste crisis. The reaction uses photocatalytic C–H bond activation to deconstruct polystyrene (PS) waste into valuable products under ambient conditions (1 bar O_2, 250 W Hg lamp) in an ethyl acetate/acetonitrile solvent system. The high surface area metal-free photocatalyst was synthesised using flow-assisted exfoliation and demonstrated high selectivity for acetophenone and PS conversion in sunlight. The study presents a promising and sustainable approach to combat plastic pollution by introducing the concept of visible light photocatalysis for polymer deconstruction. The technology offers a simple, reproducible, eco-friendly method that could significantly contribute to a circular economy to produce wealth (chemicals) from waste. Detailed characterisations, control experiments, and scavenging studies have been conducted to propose the mechanism of PS upcycling to acetophenone and benzoic acid. The photocatalytic C–H activation showcased in this study could motivate material scientists and catalysis researchers to create uncomplicated, metal-free photocatalysts that can activate other bonds with high dissociation energy, leading to the formation of crucial synthetic intermediates of industrial significance. This technology represents a crucial step towards more efficient and sustainable methods for combatting plastic pollution, highlighting the potential of green chemistry for creating sustainable solutions to environmental challenges.

Received 17th July 2023,
Accepted 14th August 2023

DOI: 10.1039/d3gc02591h

rsc.li/greenchem

Introduction

The rampant explosion of plastic pollution has necessitated the implementation of cutting-edge technological solutions aimed at transforming the waste stream of used plastics into useful and valuable chemicals.[1,2] One of the most abundant plastic materials, polystyrene (PS), has widespread use in contemporary society.[3,4] Yet, despite the advancements in its manufacturing processes, the recycling rate remains low at less than 1%.[5] It has led to a buildup of PS-based waste products in landfills, such as expanded foams, constituting a major ecological threat that demands immediate attention.[6,7] Attempts to solve this problem through pyrolysis and chemical & microbial degradation processes have been promising.[8,9] However, they still face several challenges, including compatibility with different forms of PS, such as solid PS and copolymers, and the selectivity of recycled products.[10] High production costs and low energy efficiency also limit these processes.[11]

Photocatalysis is a scientifically advanced method combining light and a catalyst to convert plastic materials to chemicals/fuel.[12,13] The technology has diverged into two main mechanisms; degradation and functionalization of plastic.[11,14] Degradation implies the fragmentation of the polymer chains of plastics into minor and less harmful constituents.[15] It is achieved by illuminating the plastic with a photocatalyst, creating reactive species such as free radicals.[16] These reactive species interact with the plastic and induce its degradation.[17] On the other hand, functionalization comprehends the alteration of the chemical structure of plastics to provide new or enhanced properties.[18] It is accomplished by exposing the plastic material to light energy in conjunction with a photocatalyst, leading to the generation of reactive species that interact with the chemical bonds of the plastic, thereby modifying its chemical composition that could result in increased degradability of the plastic.[19] The effectiveness of plastic upcycling also relies on the employed solvent system. The previous attempts at photocatalytic PS reforming used a solvent system

---

[a] *Catalysis Research Laboratory, Department of Chemistry, Indian Institute of Technology Ropar, Rupnagar, Punjab-140001, India. E-mail: rajendra@iitrpr.ac.in; Tel: +91-1881-232064*
[b] *Nanocatalysis Area Conversion and Catalysis Division, CSIR-Indian Institute of Petroleum, Dehradun-248005, India*

† Electronic supplementary information (ESI) available: Experimental procedures, detailed synthesis and characterisation of catalysts, the process of the photocatalytic reaction, N_2 adsorption profiles, image of reaction setup, Tauc plots, LSV analysis, and recycling data are provided in this section. See DOI: https://doi.org/10.1039/d3gc02591h

(benzene/acetonitrile (1 : 1)) containing the carcinogenic solvent benzene.[20] However, to promote environmentally friendly practices, it is recommended to eliminate benzene and, instead, incorporate less toxic organic solvents that can dissolve PS, such as ethyl acetate/acetonitrile.

The implementation of visible light photocatalysts, specifically g-C_3N_4, in the conversion of plastic materials has attracted interest due to its utilization of a vast portion of the solar spectrum, with an approximately 45% of visible light. g-C_3N_4, a two-dimensional material composed of nitrogen and carbon atoms, represents a promising alternative to traditional photocatalysts such as titanium dioxide (TiO_2) due to its numerous advantages.[21–23] One of the most significant advantages of g-C_3N_4 is its high light absorption in the visible spectrum, which reduces the energy demands for the photocatalytic process and promotes eco-friendliness.[24,25] Furthermore, g-C_3N_4's high electron mobility facilitates the effective transfer of electrons to reactive species, resulting in an increase in reaction rates compared to traditional photocatalysts.[26,27] The layered structure of g-C_3N_4 provides a surface for chemical reactions, leading to enhanced reaction kinetics.[28–30] Using visible light photocatalysts such as g-C_3N_4 in converting plastic materials can significantly enhance the photocatalytic process by reducing energy demands, enhancing reaction rates, and improving reaction kinetics. Furthermore, doping g-C_3N_4 with oxygen within its framework can augment its visible light absorption capabilities.[31,32] The oxygen doping enhances the catalyst's efficiency by enabling it to capture a broader range of visible light, thereby increasing its potential for effective photocatalysis.

Herein, C_3N_4 is implemented as a strategic solution for transforming waste PS into valuable chemicals. By harnessing the power of light, the developed sustainable process converts PS into high-demand products, such as acetophenone (AP) and benzoic acid (BA). Such small oxygenated aromatic compounds are crucial in industries ranging from perfumes and food flavouring to pharmaceuticals and agrochemicals.[33–36] In addition to reducing plastic pollution, transforming PS into valuable chemicals *via* photocatalysis offers a cost-effective alternative to traditional production methods.[37] The utilization of sunlight as the energy source further amplifies the economic viability of this protocol. By adopting this technology, the potential to revolutionize the handling of plastic waste can be increased. By upcycling PS into valuable chemicals and materials, not only the environmental impact of plastic could be diminished, but it also drives innovation in producing valuable goods. Implementing photocatalytic processes is a tactical step toward a sustainable and profitable future.

Experimental details

Catalyst synthesis

The graphitic carbon nitride (g-C_3N_4) was synthesized using a method previously reported.[38,39] Initially, 15 g of urea powder was crushed and placed in a capped crucible, which was heated in a muffle furnace at 550 °C for 3 h with a ramp rate of 2.5 °C per minute. The obtained material was ground, and 500 mg of g-C_3N_4 was loaded into a boat-shaped crucible situated in a 90-meter-long quartz tube with an outer diameter of 53 mm (as illustrated in Fig. 1b). One end of the tube was sealed with high-temperature glass wool, while the other end was left open. The sample was placed at the centre of the tube, an argon flow of 20 mL min^{-1} was maintained, and the temperature was kept at 600 °C for 3 h (Fig. 1a).

To create a temperature gradient in the tube, one side was cooled using water circulation (Fig. 1d), causing the material to condense over the colder side of the quartz tube (Fig. 1c). The condensed material was then treated with ethanol and distilled water to eliminate impurities, and dried overnight in a vacuum oven. This material was labelled as flow-assisted exfoliated g-C_3N_4 (F-g-C_3N_4). To synthesise high-surface-area g-C_3N_4, other exfoliation techniques such as chemical exfoliation (C-g-C_3N_4), thermal exfoliation (T-g-C_3N_4), and sonication-assisted exfoliation (S-g-C_3N_4) were also employed for comparison. The details of the synthesis and exfoliation process can be found in the ESI.† From the 500 mg of bulk g-C_3N_4, 180 mg of F-g-C_3N_4, 410 mg of C-g-C_3N_4, 230 mg of T-g-C_3N_4, and 480 mg of S-g-C_3N_4 were obtained.

Catalytic reaction

A glass beaker was taken to dissolve 100 mg of used PS in 4 ml of a binary organic solvent system comprising ethyl acetate and acetonitrile (Fig. S1a†). The PS was completely dissolved in the solvents by stirring (Fig. S1b†). Next, 30 mg of the photocatalyst was added to a round-bottom flask, and the PS-solvent mixture was transferred to the flask. The flask was filled with an oxygen-rich atmosphere by introducing oxygen *via* a balloon. The system was left to reach equilibrium in the dark for 30 minutes (Fig. S1b†). Then, the system was illuminated with light for a specific duration (Fig. S1c†). After the reaction was complete, the catalyst was retrieved from the reaction mixture *via* centrifugation, producing a clear and concentrated reaction mixture (Fig. 1d). The progress of the reaction was monitored using gas chromatography (GC), while gas chromatography-mass spectrometry (GC-MS) was used to identify the resulting products (Fig. S2†). The apparent quantum yield (AQY) values for the reaction were estimated using a previously established method.[38–40] Additional information on the photocatalytic reaction, reactor setup, conversion, selectivity, and AQY calculation can be found in the ESI.† The ESI† also provides detail on the nitro blue tetrazolium test, terephthalic acid text, and H_2O_2 detection protocol.

Results and discussion

Physicochemical characterisation

The X-ray diffraction (XRD) spectra for bulk and exfoliated g-C_3N_4 are presented in (Fig. 2a and b). The diffraction for the (002) plane for pristine g-C_3N_4 was obtained at 27.41°, indicating an interlayer stacking structure in the graphitic

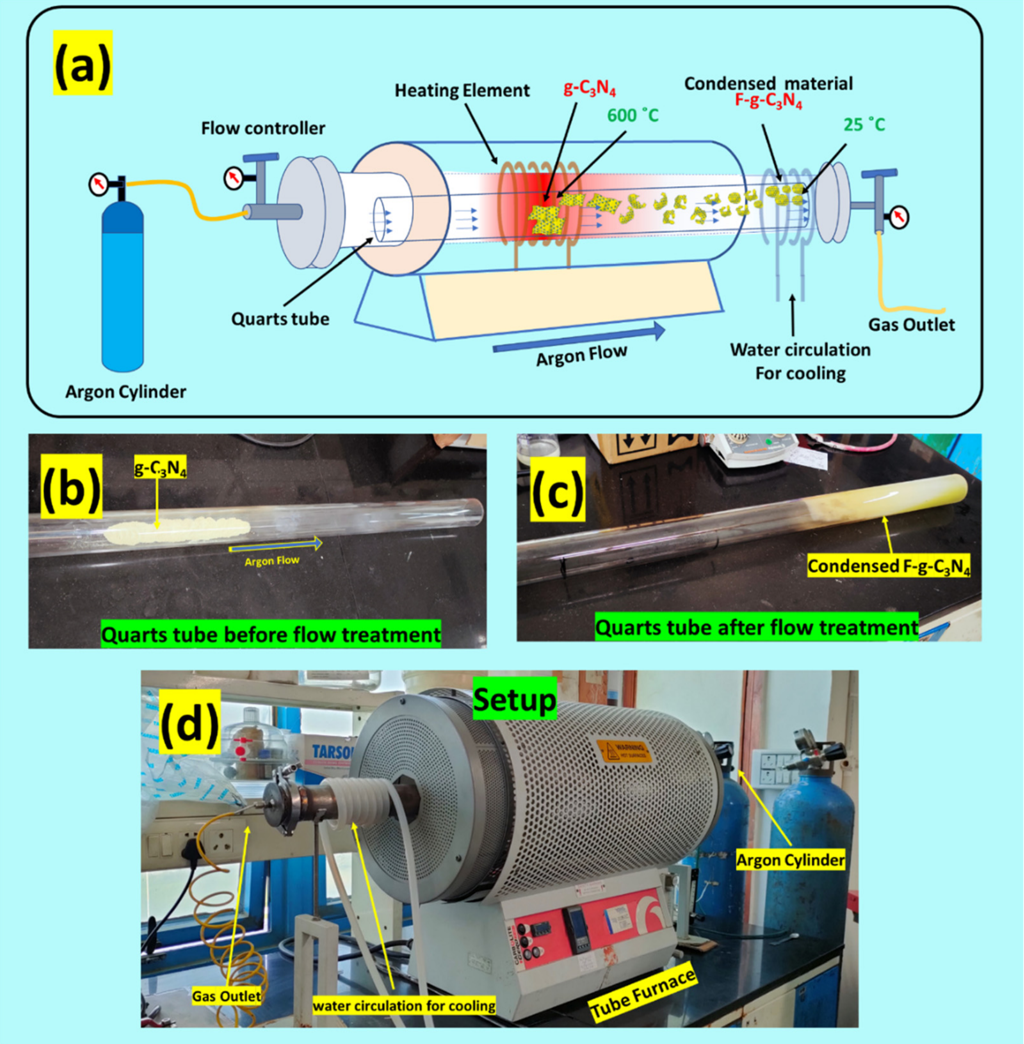

Fig. 1 (a) Photographs of the experimental set-up for the synthesis of F-g-C_3N_4 in a tube furnace, (b) digital photograph of quarts tube with material (g-C_3N_4) before inserting in tube furnace (c) digital photograph of quarts tube with material (F-g-C_3N_4) condensed over the wall of the tube after treatment, and (d) digital photograph of the setup for the synthesis of F-g-C_3N_4.

materials.[39,41] The (100) diffraction plane at approximately 13.1° provides information on the interplanar structural arrangement of the catalyst.[42] Exfoliation of the layered structure of the catalyst occurred upon sonication (designated as S-g-C_3N_4), chemical exfoliation (designated as C-g-C_3N_4), and thermal-assisted exfoliation (designated as T-g-C_3N_4), leading to broadening of the (002) diffraction peak and a simultaneous decrease in the (100) diffraction peak intensity (Fig. 2a).[43] The extent of exfoliation followed the order T-g-C_3N_4 > C-g-C_3N_4 > S-g-C_3N_4, with the degree of broadening decreasing in the same order (Fig. 2a). Moreover, the (002) peak in C-g-C_3N_4 shifted to a lower angle value, while in T-g-C_3N_4 and S-g-C_3N_4, it shifted to a higher angle value, indicating an increase and decrease in the inter-layer spacing, respectively (Fig. 2b).[44] The XRD pattern of F-g-C_3N_4 is similar to pristine g-C_3N_4; the (100) peak almost disappeared, probably due to the replacement of nitrogen with oxygen, discussed later in X-ray photoelectron spectroscopy (XPS) analysis.[45,46] The substitution disrupted the ordered stacking of tri-*s*-triazine rings, reducing the nanosheets' planar size and a less ordered stacking of tri-*s*-triazine rings. The less pronounced (100) peak in F-g-C_3N_4 is also attributed to this disruption.[47] The loose stacking between the layers of exfoliated g-C_3N_4 sheets is consistent with the slightly negative shift of the (002) peak observed in F-g-C_3N_4 in Fig. 2b, indicating a larger interlayer spacing.[48]

The thermogram shown in Fig. 2c indicates that pristine g-C_3N_4 remains thermally stable up to 500 °C in N_2. Therefore, thermal exfoliation was conducted at 500 °C in a static argon atmosphere using a tube furnace. The material exhibited weight loss after reaching 550 °C in TGA analysis and was entirely degraded at 701 °C (Fig. 2c). To perform flow-assisted exfoliation of g-C_3N_4, a tube furnace was employed with argon flow of 20 mL min^{-1} at 600 °C. At this temperature, the g-C_3N_4

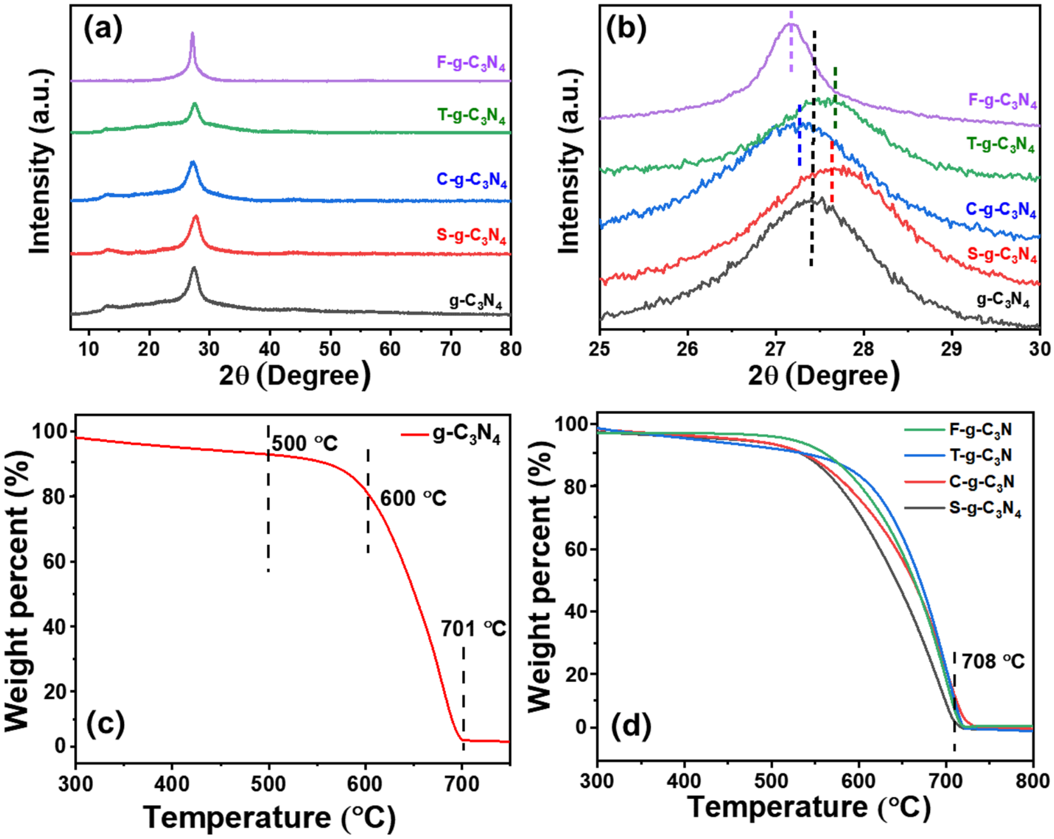

Fig. 2 (a) Powder XRD patterns of all g-C_3N_4 based photocatalysts synthesised for this study, (b) magnified powder XRD patterns of all g-C_3N_4 based photocatalysts synthesised for this study, (c) thermograms of pristine g-C_3N_4 in N_2 gas, and (d) thermograms of all exfoliated photocatalysts in N_2 gas.

sheets unfolded and flowed with the Ar gas. The middle part of the quartz tube was heated while the corners were kept cold. As the sheets moved towards the colder area of the tube, they self-assembled into a spherical foam nanostructure (Fig. 1a), which condensed over the cold wall in the quartz tube (Fig. 1c). Furthermore, the TGA analysis of all exfoliated photocatalysts exhibited similar thermal stability as pristine g-C_3N_4 (Fig. 2d) and completely decomposed at <710 °C.

Textural properties such as morphology and surface area (Table S2) and (Fig. S4†) were evaluated using FESEM and N_2-adsorption analysis. The FESEM images of pristine and exfoliated g-C_3N_4 photocatalysts were recorded at various magnifications (Fig. 3a–f). Pristine g-C_3N_4 exhibited an aggregation of flakes and a nonporous architecture (Fig. 3a).[49] The BET analysis revealed a surface area of 38 $m^2\ g^{-1}$ for urea-derived g-C_3N_4.[50] On the other hand, sonicated g-C_3N_4 demonstrated less aggregation compared to pristine g-C_3N_4, indicating that the sonication partially opened the g-C_3N_4 layers (Fig. 3b).[51] The stretching of the layers resulted in an increased surface area of 61 $m^2\ g^{-1}$. Chemically treated g-C_3N_4 showed a sponge-like three-dimensional framework with an interconnected porous structure (Fig. 3c).[52] The H_2SO_4 etching caused the breaking of hydrogen bonds between the g-C_3N_4 layers, leading to the insertion of water molecules, which caused g-C_3N_4 to swell and acquire a spongy architecture with a surface area of 126 $m^2\ g^{-1}$.[48,52] The SEM images of the thermally exfoliated photocatalyst indicated thinner and more dispersed layers of the material (Fig. 3d), which resulted from the separation of the stacked layers of g-C_3N_4 sheets caused by high-temperature treatment.[39] This separation raised the surface area of the material to seven times its original value (227 $m^2\ g^{-1}$). FE-SEM images of F-g-C_3N_4 show that the self-assembly of sheets of g-C_3N_4 into a spherical architecture occurred after exfoliation (Fig. 3e and f). In flow-assisted exfoliation, the nanosheets flowed with Ar from the hot part to the cold part of the tube. Due to the temperature gradient, the nanosheets self-assembled into spherical form by self-enveloping to form spheres.[46] These spheres condensed into spheres at the colder part of the tube (Fig. 1c). The thermal treatment unwrapped the sheets, breaking them into different sizes. Thus, the size of the flowing sheets was non-uniform, leading to non-uniformity in the size of spheres, as seen in the SEM images (Fig. 3l). The small size sheets did not self-envelope into the spheres but remained as small nanosheets in the material. Transforming sheets into nanospheres of different sizes increased the surface area to 177 $m^2\ g^{-1}$. Textural properties determined from N_2-sorption isotherms (Fig. S4†) are summarized in Table S2.†

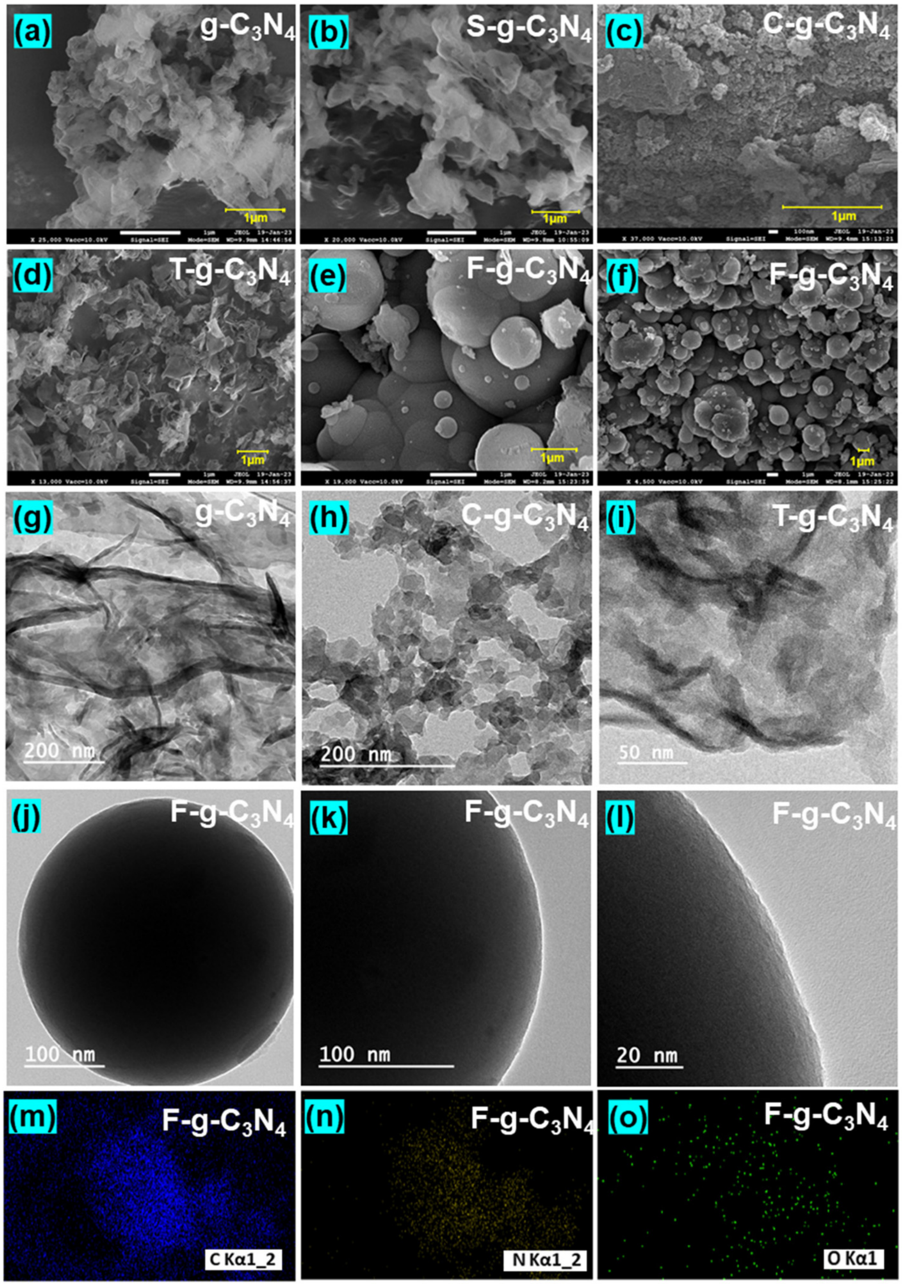

Fig. 3 FESEM images of (a) g-C_3N_4, (b) S-g-C_3N_4, (c) C-g-C_3N_4, (d) T-g-C_3N_4, and (e & f) F-g-C_3N_4, HRTEM images of (g) g-C_3N_4, (h) C-g-C_3N_4, (i) T-g-C_3N_4, and (j, k & l) F-g-C_3N_4, and (m, n & o) elemental mapping of F-g-C_3N_4.

HRTEM analysis was conducted for g-C_3N_4 and all the exfoliated catalyst samples (Fig. 3g–l). The g-C_3N_4 material displayed a sheet-like morphology with a nonporous structure (Fig. 3g). In contrast, C-g-C_3N_4 exhibited more segregated sheets, indicating a higher degree of sheet separation (Fig. 3h). T-g-C_3N_4, which underwent thermal exposure, showed comparably less aggregation than g-C_3N_4, suggesting that the thermal treatment caused the catalyst layers to open up (Fig. 3i). The flow-assisted exfoliation process employed in F-g-C_3N_4 resulted in the formation of spherical structures through the self-assembly of the layers, as discussed previously (Fig. 3j–l). The TEM images demonstrate that the spheres are solid composition rather than hollow. The porosity is due to interparticle porosity generated due to aggregation of nanospheres (Fig. 3k). Additionally, elemental mapping using energy-dispersive X-ray spectroscopy (EDX) confirmed that F-g-C_3N_4 consisted of carbon, nitrogen, and oxygen elements (Fig. 3m–o).

X-ray photoelectron spectroscopy (XPS) was conducted to determine the chemical composition of g-C_3N_4 and F-g-C_3N_4 (Fig. 4). The XPS survey of pristine g-C_3N_4 and F-g-C_3N_4 revealed peaks corresponding to the elements N, C, and O (Fig. 4a). However, the peak intensity for O 1s in F-g-C_3N_4 was

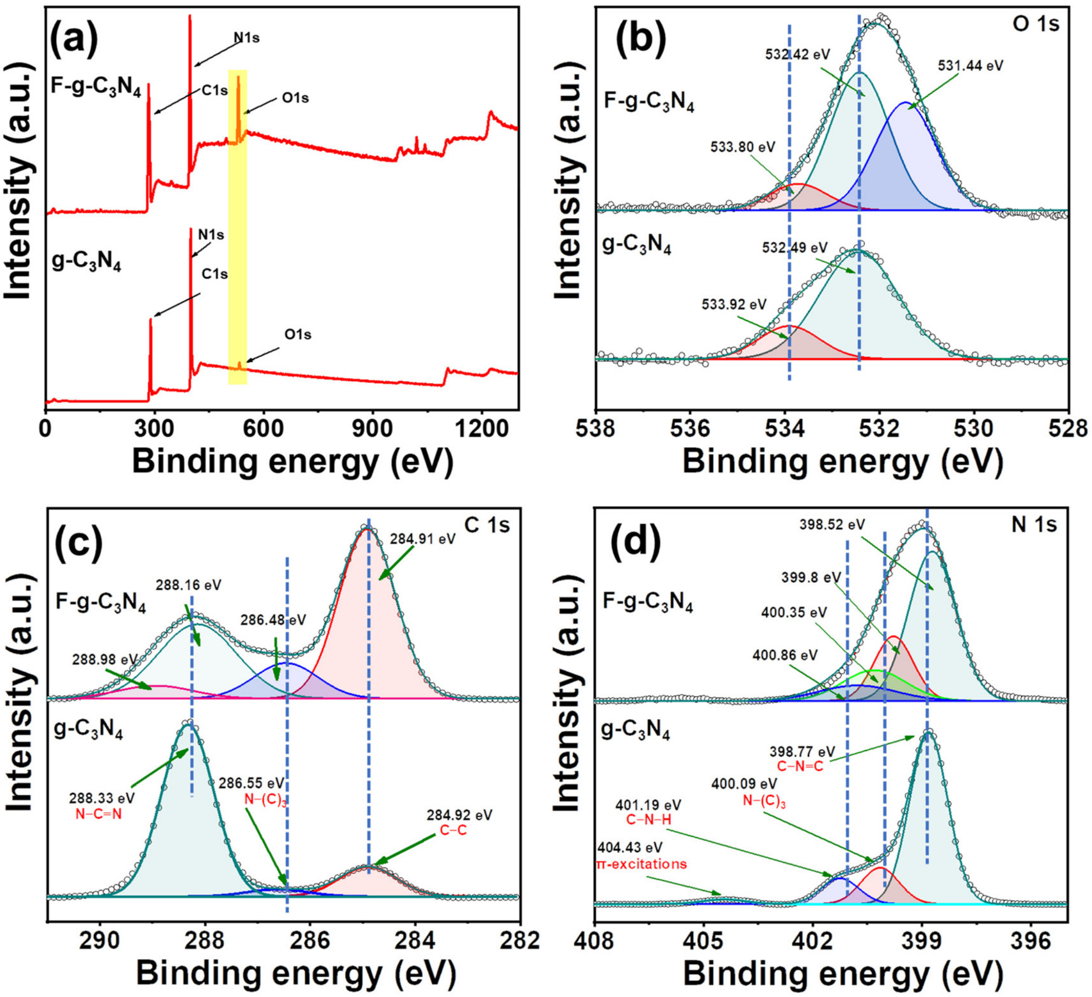

Fig. 4 (a) XPS survey of pristine g-C_3N_4 and F-g-C_3N_4, (b) high-resolution O 1s XPS spectra of g-C_3N_4 and F-g-C_3N_4 (c) high-resolution C 1s XPS spectra of g-C_3N_4 and F-g-C_3N_4, and (d) high-resolution N 1s XPS spectra of g-C_3N_4 and F-g-C_3N_4.

higher than pristine g-C_3N_4 (Fig. 4a, yellow area), indicating a higher surface concentration of O atoms in F-g-C_3N_4. The high-resolution O 1s spectra (Fig. 4b) showed two types of O atoms in pristine g-C_3N_4, with corresponding binding energies of 532.49 eV (O–H) and 533.92 eV (O–N).[53] The 532.49 eV peak in pristine g-C_3N_4 was due to surface hydroxyl groups, while the 533.92 eV peak resulted from intermediates generated during thermal polymerisation. In contrast, a prominent peak at a lower binding energy (531.1 eV) was observed in the XPS spectrum of O 1s for F-g-C_3N_4, attributed to oxygen in the form of N–C–O and C–O bonding.[46,53,54] It confirms the O-doping in F-g-C_3N_4, where O atoms are bonded to C atoms (Fig. 4b).[46] The C 1s spectrum of pristine g-C_3N_4 (Fig. 4c) showed three types of carbon, with peaks located at 284.92 eV (sp^3 carbon or C–C), 286.55 eV (C–N), and 288.33 eV (N–C–N), indicating the diverse carbon species.[38,39,46,55] On the other hand, the C 1s spectrum of F-g-C_3N_4 showed an additional peak at a higher binding energy of 288.98 eV, indicating the formation of N–C–O bonds (Fig. 4c). It confirms that O atoms were incorporated into the *s*-triazine unit of g-C_3N_4 by bonding with C atoms.[46] To determine the exact location of oxygen atoms in the *s*-triazine matrix, an analysis of the N 1s spectra of pristine g-C_3N_4 and F-g-C_3N_4 was conducted (Fig. 4d). Peaks for N atoms at 401.19 eV in g-C_3N_4 and 400.86 eV in F-g-C_3N_4, correspond to surface amino groups.[38,39,55,56] The deconvoluted XPS signal at 400.09 eV and 398.77 eV indicate di-coordinated (C–N–C) and tri-coordinated (N–$(C)_3$) nitrogen in g-C_3N_4, respectively.[38,39,46,55,56] The ratio of di-coordinated and tri-coordinated N atoms slightly decreased in F-g-C_3N_4. Additionally, the binding energy of tri-coordinated and di-coordinated N atoms shifted from 400.09 eV (pristine g-C_3N_4) to 399.8 eV and 398.77 eV (pristine g-C_3N_4) to 398.52 eV, respectively, due to the introduction of O atoms into the aromatic system.[46] Thus, it is evident that the doped O atoms are explicitly bonded to C atoms, replacing di-coordinated N atoms. The surface elemental analysis determined from XPS shows that the N/C ratio is lower in F-g-C_3N_4 than in g-C_3N_4, confirming that "O" was doped at "N" sites.[46] This observation was consistent with bulk elemental composition determined from CHNSO (Table S3†). Moreover, the content of O (determined from CHNSO and XPS) is more in F-g-C_3N_4 than in g-C_3N_4, further confirming this result (Table S3†). Notably, F-g-C_3N_4 exhibited a distinct peak at a binding energy of 400.35 eV in Fig. 4d, which can be attributed to the presence of cyano terminal groups (C≡N).[46] During high-temperature thermal treatment, some of the C–N bonds undergo cleavage, leading to the reconstruction of the material and the simultaneous formation of C≡N bonds and O-doping. The presence of C≡N was also confirmed through FTIR analysis, where a distinct peak was observed at ∼2210 nm in the FTIR spectrum of F-g-C_3N_4 (Fig. S5†).[46] The FTIR characterization also ruled out the –COOH groups. Furthermore, XPS analysis of other exfoliated catalysts (T-g-C_3N_4 and C-g-C_3N_4) displayed a similar pattern to pristine g-C_3N_4, albeit with slight shifts in the peak positions (Fig. S6†).

Different samples, F-g-C_3N_4 and T-g-C_3N_4, were obtained from the bulk g-C_3N_4 material by subjecting it to distinct heat treatment. F-g-C_3N_4 was produced by heating the bulk g-C_3N_4 at 600 °C for 3 h in an argon (Ar) flow, while T-g-C_3N_4 was obtained by heating it at 500 °C for 3 h under static Ar conditions. The subsequent procedures for both samples were the same. During the exfoliation process at high temperatures, it is likely that oxygen released during heating incorporated into the g-C_3N_4 framework. Moreover, oxygen impurities in the 99% pure Ar gas may have been incorporated into F-g-C_3N_4 to a greater extent at 600 °C compared to the doping in T-g-C_3N_4 at 500 °C under static Ar conditions. To further investigate this phenomenon, bulk g-C_3N_4 was heated at the same temperature in a vacuum instead of an Ar flow, resulting in V-g-C_3N_4, which exhibited a pale white colour and showed weak absorption in the UV region (Fig. S7a†). The XPS surface survey spectrum of V-g-C_3N_4 indicated minimal oxygen presence (Fig. S7b†). These observations suggest that oxygen doping occurred in F-g-C_3N_4 during the exfoliation process in the Ar flow, despite the presence of air impurities in the Ar gas.

Optical properties analysis

Solid-state ultraviolet-visible spectra were recorded to assess the light absorption properties of the photocatalysts.[57,58] The results indicate that pristine g-C_3N_4 exhibited an absorption covering the visible region (Fig. 5a). The exfoliated g-C_3N_4 materials, except for F-g-C_3N_4, displayed a significant blue shift. F-g-C_3N_4, in particular, showed a redshift, possibly due to oxygen doping (discussed in XPS), which resulted in dark green colour (Fig. S8†).[46] The finding indicates that F-g-C_3N_4 has an increased visible light absorption capacity, making it more efficient for photocatalytic reactions under visible light irradiation. The Tauc plots were utilized to determine the band gap (ESI†). The F-g-C_3N_4 possessed a narrow band gap (2.4 eV), while a broad band gap of 2.8 eV originated in C-g-C_3N_4 (Fig. S9†). Photocatalysts with narrow band gaps are primarily active in visible light, making F-g-C_3N_4 preferable photocatalyst for visible light applications.[59]

The photoluminescence (PL) spectra were recorded to determine their effective charge separation (Fig. 5b). PL analysis was performed with an excitation wavelength of 340 nm.[38] Pristine g-C_3N_4 showed an extensive peak at the visible region with a peak maximum of 468 nm.[60] In contrast, exfoliated catalysts showed narrow spectra with lower peak intensity. S-g-C_3N_4 had a narrow emission peak than pristine g-C_3N_4, indicating better charge retention.[61] T-g-C_3N_4 exhibited comparatively lower emissions during PL analysis than g-C_3N_4 and S-g-C_3N_4. Moreover, the emission peak corresponding to C-g-C_3N_4 showed a slight blue shift with a peak maximum at 457 nm, attributed to a broad band gap of C-g-C_3N_4.[62] F-g-C_3N_4 showed the broad emission peak with lower intensity, indicating a comparatively lower electron and hole recombination rate. Additionally, the peak maximum of the emission peak shifted towards a higher wavelength, corresponding to a red shift in the PL spectra due to the narrowing of the band gap. It is anticipated that introducing oxygen into the g-C_3N_4 framework generated sites that trap electrons and facilitated forming of doping levels within the conduction band of g-C_3N_4.[63] As a consequence, the separation of charge carriers caused by light irradiation and the reduction of the band gap is expected to be more efficient.[46,64]

Further investigation was carried out to examine the photoluminescence (PL) decay characteristics of both pristine and exfoliated g-C_3N_4, utilizing time-correlated single photon counting (TCSPC) (ESI†). The results demonstrated a specific trend in the average lifetime, namely T-g-C_3N_4 > C-g-C_3N_4 > S-g-C_3N_4 > g-C_3N_4 > F-g-C_3N_4 (Table S4†). A comparison between pristine g-C_3N_4 and F-g-C_3N_4 revealed a reduction in both the shorter lifetime (τ_1) and longer lifetime (τ_2) (from 0.8 to 0.5 ns and 4.0 to 3.0 ns, respectively) (Table S4†). Consequently, the average lifetime decreased from 3.0 ns (g-C_3N_4) to 2.4 ns (F-g-C_3N_4) (Table S4†). Moreover, the contribution of the shorter lifetime dropped from 31% to 22%, while that of the longer lifetime rose from 69% to 78% (Table S4†). The shorter lifetime is linked to the radiative decay from the excited state to the ground state.[46,65] The reduction in the contribution of the shorter lifetime suggests a decreased quantity of rapidly recombined charge carriers. The decrease in the average lifetime and changes in the contributions indicate that there was more nonradiative transfer of photogenerated charge carriers in F-g-C_3N_4.[46,66] It could imply that the nanospheres shortened the transfer distance of charge carriers.

Photoelectrochemical analysis

Linear sweep voltammetry (LSV) was conducted under dark and illuminated conditions (Fig. S10a and b†). For the g-C_3N_4 catalyst, the photocurrent density showed a reasonable increase with respect to the applied potential in both dark and illuminated conditions. Notably, under light illumination, the current density of g-C_3N_4 was higher, reaching 154×10^{-6} A cm^{-2}, compared to its dark conditions (current density of 107×10^{-6} A cm^{-2}), indicating its good photochemical activity in light.[67] The flow-assisted exfoliation of g-C_3N_4 resulted in a significant improvement in photocurrent density under both dark (184×10^{-6} A cm^{-2}) and light (264×10^{-6} A cm^{-2}) conditions, thus demonstrating its superior capacity to generate

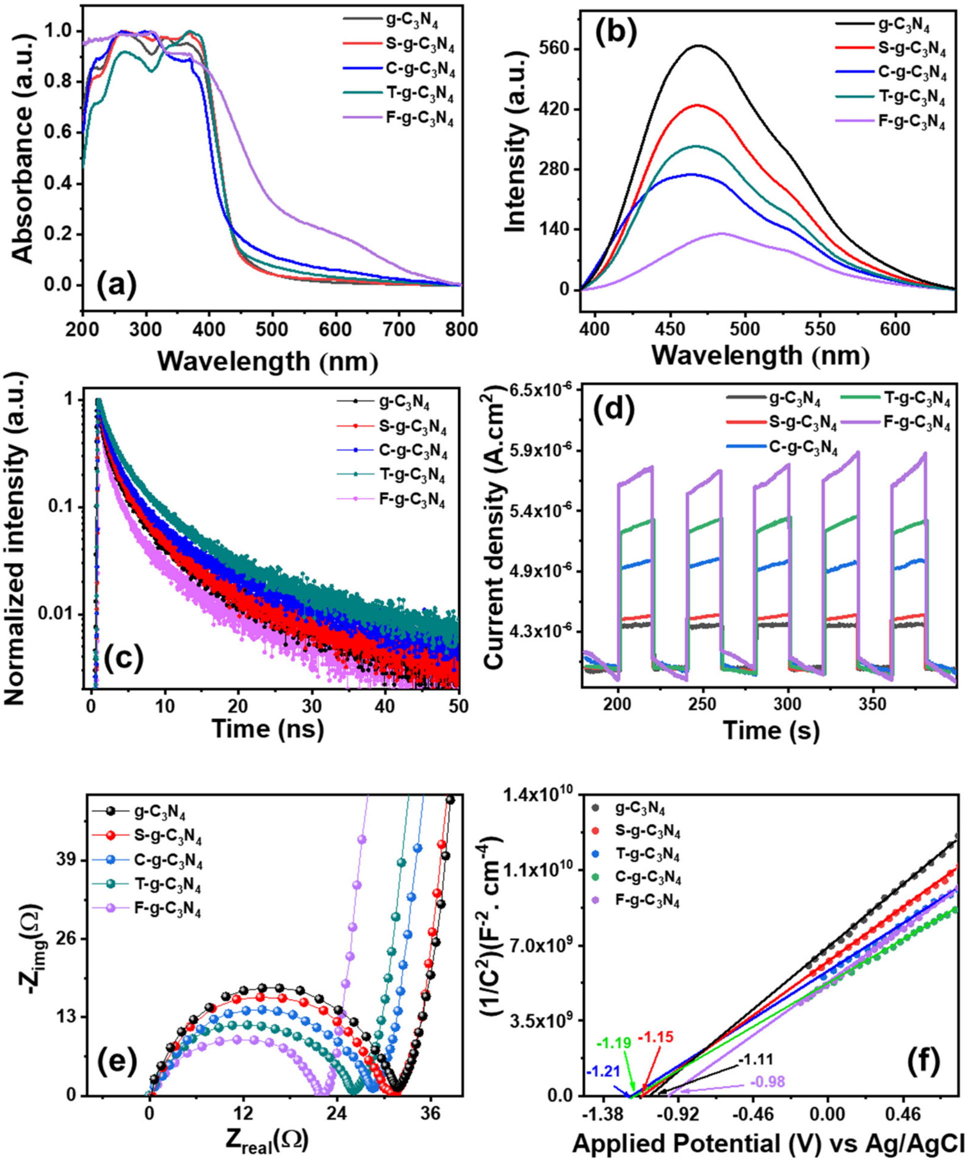

Fig. 5 (a) Ultraviolet-visible absorption spectra, (b) photoluminescence spectra, (c) time-resolved decay of photoluminescence, (d) response of transient photocurrent, (e) impedances of electrochemical nature, (f) plots of Mott–Schottky analysis for different photocatalysts.

and transfer charge carriers.[38] The highest photocurrent density was observed for F-g-C_3N_4 over the applied potential, indicating better ejection of electron and hole pairs with good photo absorption capability.

Furthermore, the pristine and exfoliated photocatalysts underwent a comprehensive analysis of their photoresponses using an on–off photocurrent investigation (Fig. 5d). The observed behavior indicated a marked increase in current density when the catalyst was exposed to light, which reverted to the initial state once the light was turned off. The response current of all the photocatalysts was scrutinized precisely over several test rounds to ensure stability in the response current. The results confirmed that all the catalysts demonstrated consistent response current in every test cycle. Notably, all the exfoliated photocatalysts displayed a better current response than pristine g-C_3N_4. The F-g-C_3N_4 showed the most impressive photocurrent response, followed by T-g-C_3N_4, C-g-C_3N_4, S-g-C_3N_4, and g-C_3N_4. These findings indicate that F-g-C_3N_4 and T-g-C_3N_4 are highly photochemically active.[66] The hike in response current can be attributed to an upsurge in conductivity, as the conductivity (σ) of a material is directly proportional to the number of charge carriers (N) and their mobility (μ) ($\sigma = Ne\mu$).[68] Therefore, it can be summarized that the exfoliated F-g-C_3N_4 and T-g-C_3N_4 generated more charge carriers upon light illumination than the other examined photocatalysts.

Electrochemical impedance spectroscopy (EIS) is a technique that enables the investigation of the properties of the interface between an electrode and an electrolyte system, with particular emphasis on the charge transfer characteristics. EIS of all the material was subsequently analyzed by fitting them into Nyquist plots shown in Fig. 5e. A semicircle is visible and directly correlates with the charge transfer rate.[69] The diameter of the semicircle arc reflects the interfacial charge transfer resistance (R_{ct}).[70] All the exfoliated catalysts exhibited lower semicircle diameters (R_{ct}) than g-C_3N_4, indicating an efficient electron and hole separation.[71] F-g-C_3N_4 showed the smallest R_{ct} value of all the exfoliated catalysts, suggesting its superior photoactivity.

Band structure analysis

The results of Mott–Schottky (MS) analyses have been employed to investigate the photocatalysts' band edges (ESI†).[72–76] E_{fb} values of the three exfoliated catalysts (S-g-C_3N_4, T-g-C_3N_4, and C-g-C_3N_4) showed a slight upward shift, while F-g-C_3N_4 exhibited a small downward shift in the potential (Fig. 5f). It is attributed to oxygen doping in F-g-C_3N_4 that occurred during the exfoliation process. Furthermore, the E_{CB} values were calculated using E_{fb} values obtained from Mott–Schottky plots. The E_{CB} was consistent across all the photocatalysts, ranging from 1.69 to 1.74 *vs.* NHE (Table S5†).

The complete band structures of the materials were scrutinized through a comprehensive analysis of valence band X-ray photoelectron spectroscopy (VB-XPS), ultraviolet photoelectron spectroscopy (UPS), and diffuse reflectance UV-visible spectroscopy (Fig. 6).[38,39] The VB-XPS analysis of pristine g-C_3N_4 and F-g-C_3N_4 revealed that their valence band maxima (VBM) were located at 1.49 eV and 1.63 eV, respectively, concerning their Fermi levels (E_f).[77] The E_f of g-C_3N_4 and F-C_3N_4 was associated with their work function Φ, which refers to the energy difference between the E_f and vacuum.[78] UPS analysis provided additional insight into the work function Φ values for g-C_3N_4 and F-C_3N_4, estimated to be 4.70 eV and 4.51 eV, respectively, utilizing the relationship $\Phi = 21.22 - E_{\text{SEcut off}} + E_{\text{cutoff}}$.[79] Furthermore, by integrating the data obtained from VB-XPS, DRUV-vis, and UPS spectra, the E_{CB} and E_{VB} values of g-C_3N_4 were 6.19 eV and 3.44 eV, respectively, in relation to vacuum. The E_{CB} and E_{VB} values of F-C_3N_4 were 6.14 eV and 3.55 eV, respectively. The band edge values were expressed in E_{vac} and were converted to E_{NHE} through the addition of −4.44 ± 0.02 eV.[80] The band structures of the other exfoliated catalysts were also determined by a similar method (Fig. S11†). The calculated band structures for all the photocatalysts are shown in Fig. 6e, and the band edges determined through this approach were found to align well with the band structure estimated from the MS plots, with a slight shift. In addition, the work function was determined for all the photocatalysts, and it was discovered that g-C_3N_4 had the highest work function while F-g-C_3N_4 had the lowest. It implies that photogenerated electrons can more effortlessly move to the surface of the photocatalyst, where they can participate in the photocatalytic reaction, in the case of F-g-C_3N_4.[37] Thus, F-g-C_3N_4 could be the most active photocatalyst among all the analyzed photocatalysts due to its lower work function.

Photocatalytic activity

The photocatalytic oxidation of waste PS was meticulously conducted utilizing the pristine g-C_3N_4 in an oxygen-rich environment of 1 bar for 8 h. The initial step towards optimal reaction involved the optimization of the catalyst amount. Ultimately, the finest activity was recorded using 30 mg of photocatalyst, leading to a 27.6% conversion (Fig. 7a) with 90.8% selectivity of AP and 9.2% of BA. Hereafter, the photocatalyst quantity was set at 30 mg for subsequent reactions. To fine-tune the light source, photocatalytic oxidation was carried out utilizing different light sources. Results from the experiment show that the catalyst was most active in a 250 W Hg lamp (Fig. 7b). Moreover, when exposed to sunlight, the conversion was even more pronounced, with a PS conversion rate of 38.6% recorded in 8 h (4 h + 4 h, in two consecutive days) with 86.7% selectivity of AP and 13.3% of BA. Conversely, employing a household 20 W LED resulted in a little PS conversion of 3.4%. In conclusion, based on the experiment results, the 250 W Hg lamp and sunlight were the most effective light sources for this reaction, with the former being utilized for further optimization.

The oxygen atmosphere was chosen for the reaction due to its capacity to abstract electrons from the photocatalyst, creating superoxide and catalyzing the PS oxidation.[81] The mechanism of this process will be discussed later. To further determine the effect of the atmosphere on the reaction, the experiments were conducted in distinct atmospheres, including air and an inert argon atmosphere. Subsequently, PS oxidation was initiated within the Ar gas-filled reaction vessel. However, the PS conversion rate in the Ar atmosphere dropped to 0.5%, indicating the considerable contribution of O_2 in the reaction (Fig. 7c). In contrast, when the reaction was performed in the air atmosphere, the photocatalyst's activity was lower than that in the O_2 atmosphere, proving the pivotal part of O_2 in the PS oxidation (Fig. 7c).

The efficacy of g-C_3N_4 in PS oxidation was deficient. However, increasing the catalyst's surface area presents a probable strategy to improve its activity. The initial methodology employed towards this objective was the hard template technique, wherein mesoporous g-C_3N_4 was synthesized employing SBA-15 as a template.[82] Despite this, the outcome yielded a marginal increment in photocatalytic activity during PS oxidation with meso-g-C_3N_4 (Fig. 7d), affording 40.2% PS conversion. Consequently, exfoliation was endorsed to raise the surface area of the g-C_3N_4.[39]

This study employed various techniques to exfoliate the catalyst (as discussed in the experimental section). S-g-C_3N_4 showed only a marginal increase in PS conversion. However, with the same reaction conditions, 35.6% of PS was consumed in the photocatalytic PS reforming, with 89.2% selectivity of AP and 10.8% of BA. This outcome motivated us to investigate other exfoliation methods to enhance the catalyst's activity for the reaction. C-g-C_3N_4 demonstrated better activity, yielding a 42.1% PS conversion with 86.6% selectivity of AP and 13.4% of BA. T-g-C_3N_4 exhibited a PS conversion of 54.6%, surpassing all other catalysts. F-g-C_3N_4 displayed the highest activity, with

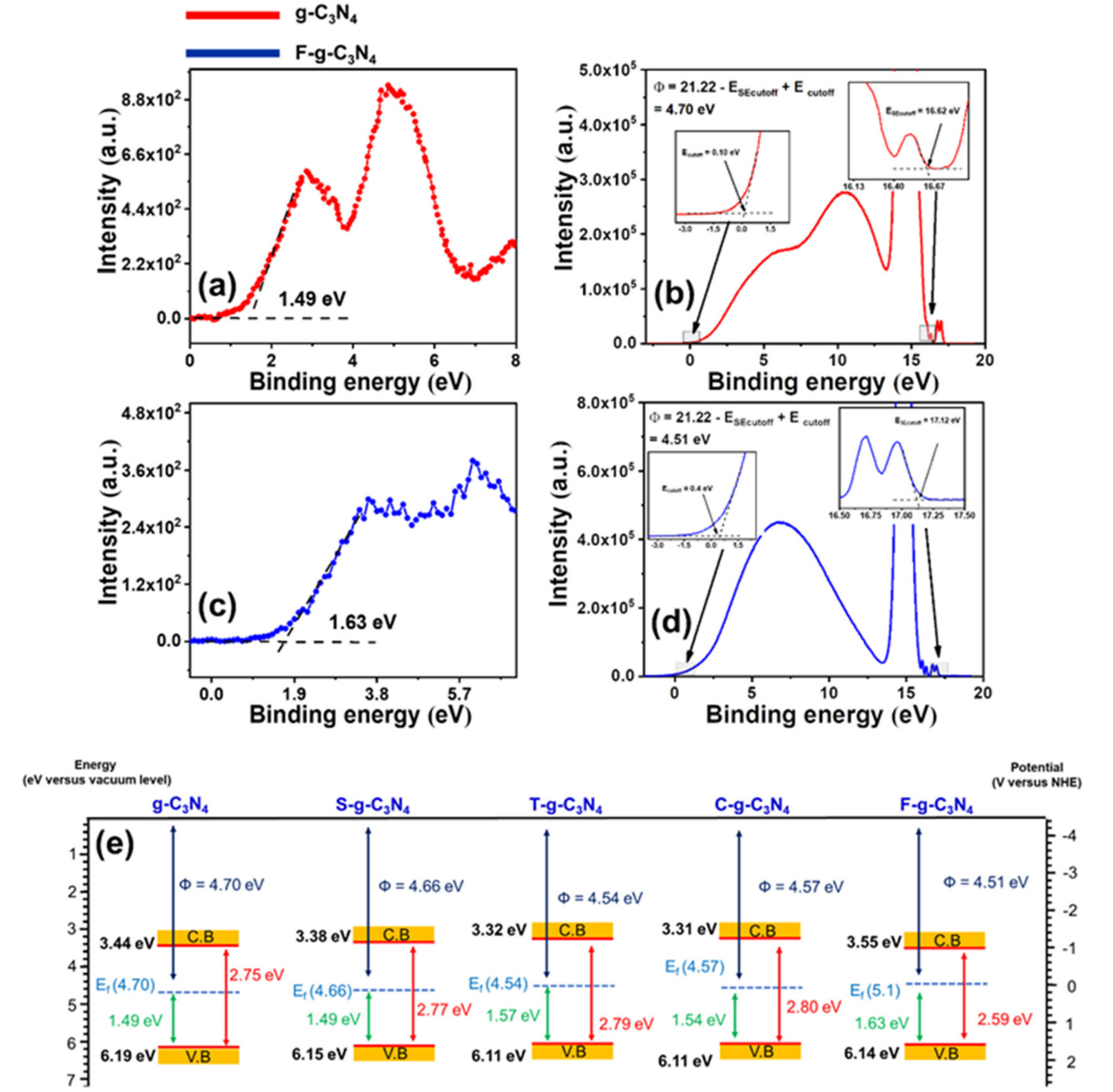

Fig. 6 (a) VB-XPS spectrum of g-C_3N_4, (b) UPS spectrum of g-C_3N_4, (c) VB-XPS spectrum of F-g-C_3N_4 (d) UPS spectrum of F-g-C_3N_4, and (e) band structures of photocatalysts of this study.

a 68.8% PS conversion, 82.1% selectivity of AP, and 17.9% for BA with an AQY value of 59×10^{-2} (Table S6†). Consequently, the reaction in sunlight using this catalyst showed an 81% PS conversion, with 77.5% selectivity of AP and 22.5% of BA. The AQY value over all the catalysts is included in Fig. 7d and Table S6.†

The photocatalytic PS reforming has been attempted using a solvent system (benzene/acetonitrile (1 : 1)), which includes the carcinogenic solvent benzene. To make the process environmentally friendly, it was necessary to avoid using benzene. Therefore, various solvent systems were tested, all of which were capable of dissolving PS. Among these solvent systems, the ethyl acetate/acetonitrile (EA/ACN) system was found to be the most effective (Table 1). Consequently, all possible variations of the EA/ACN solvent system were tested. The most promising result was obtained with the (1 : 0.142) EA/ACN ratio, which yielded a PS conversion of 63.2%, with 86.2% selectivity for AP and 13.8% for BA. Although the conversion was 5% lower than that obtained with the benzene-containing solvent system, avoiding benzene and opting for a greener solvent is preferable. It makes the process more efficient in terms of sustainability. The broad applicability of the photocatalytic oxidation process is demonstrated for the oxidation of various organic molecules under similar reaction conditions. A comparison table containing the results of these experiments is included in the ESI section of the manuscript (Table S7†).

Gel Permeation Chromatography (GPC) was performed on both polystyrene (PS) and the remaining polymer after the reaction (Table 1, entry 11). The number average molecular weight (Mn) of PS was 72 096 g mol^{-1}, while the Mn of the remaining polymer was 21 913 g mol^{-1}. These results indicate that the polymer underwent successful degradation to a large

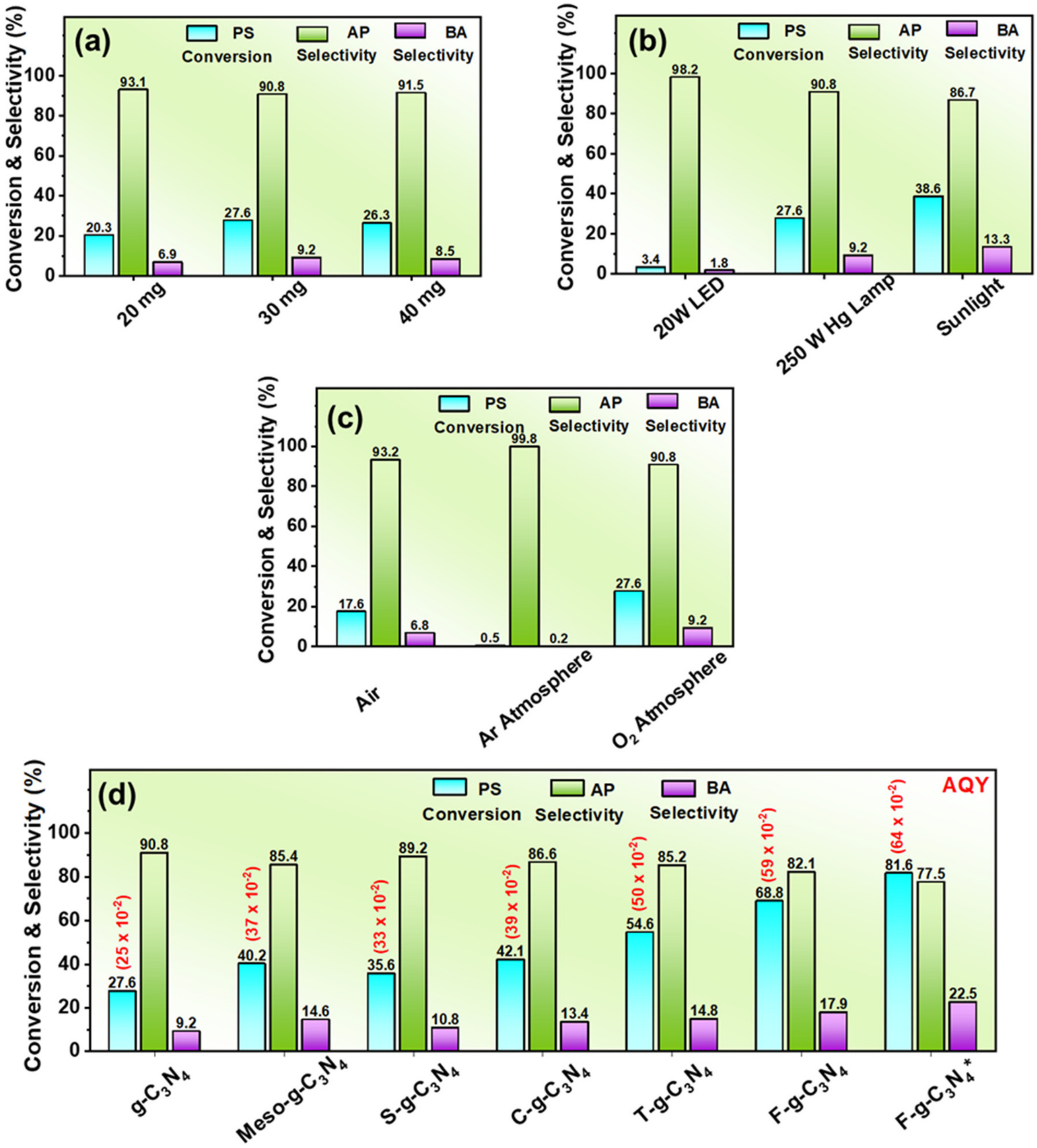

Fig. 7 Photocatalytic PS oxidation with variation in (a) catalyst amount, (b) light source, (c) reaction atmosphere, and (d) photocatalyst. (Reaction conditions: photocatalyst (30 mg), light source (250 W Hg lamp), PS (104 mg), solvent (benzene : acetonitrile (1 : 1) (4 ml)), and O_2 1 bar.)

extent. FTIR analysis was conducted to determine the identity of the remaining polymer. The FT-IR spectra of polyethylene (PE), the remaining polymer, and PS were compared (Fig. S12†). Upon comparison, it was observed that the FT-IR spectra of the remaining polymer did not match with PE. Instead, it exhibited a resemblance to PS, although with reduced band intensities. The finding suggests that the remaining polymer was unreacted or un-degraded PS. The reduced Mn confirmed by GPC supports this conclusion.

While previous studies have explored the photocatalytic degradation of polystyrene derived from used plastics, to the best of our knowledge, there is a lack of specific reports focusing on the application of heterogeneous photocatalysts for the room temperature upcycling of plastic-based polystyrene. However, to provide a broader context for this research, comparative data (Table S8†) has been included in the ESI†.[20,26,83–87]

The investigation of the kinetics of the PS conversion reaction was conducted to acquire a deeper understanding of the photocatalytic process. The application of first-order kinetics led to a linear graph of PS conversion plotted against time (Fig. 8a), providing the means to determine the rate constant

Table 1 Solvent variation for the photocatalytic PS reforming

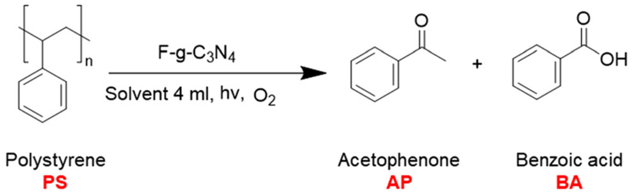

Entry	Solvent	PS conversion	AP selectivity	BA selectivity	AQY
1	Benzene	~4	97.2	2.8	3×10^{-2}
2	Acetonitrile	~0	—	—	—
3	Ethyl acetate	22.5	93.2	6.8	19×10^{-2}
4	Acetone	~0	—	—	—
5	Benzene : acetonitrile (1 : 1)	68.8	82.1	17.9	59×10^{-2}
6	Acetone : ethyl acetate (1 : 1)	~5	96.1	3.9	4×10^{-2}
7	Acetone : acetonitrile (1 : 1)	~0	—	—	—
8	Ethyl acetate : acetonitrile (1 : 3)	6.8	95.2	4.8	6×10^{-2}
9	Ethyl acetate : acetonitrile (1 : 1)	12.5	94.1	6.9	11×10^{-2}
10	Ethyl acetate : acetonitrile (1 : 0.33)	42.5	92.2	7.8	37×10^{-2}
11	Ethyl acetate : acetonitrile (1 : 0.142)	63.2	86.2	13.8	54×10^{-2}
12	Ethyl acetate : acetonitrile (1 : 066)	35.5	90.1	9.9	30×10^{-2}
11[a]	Ethyl acetate : acetonitrile (1 : 0.142)	72.8	81.6	18.4	57×10^{-2}

Reaction conditions: photocatalyst (30 mg), light source (250 W Hg lamp), PS (104 mg), solvent (4 mL)), time (8 h), and O_2 (2 bar). [a] Reaction in sunlight.

(k), which was calculated to be 4.26×10^{-5} s^{-1}. Since the PS oxidation is photocatalytic, kinetics relies on light source intensity. Accordingly, the reaction was carried out under varying light intensities (Fig. S13b†), and plots of ln[PS conc] *versus* time were produced. Analysis of the resulting kinetic plots (Fig. 8a) showed a decline in k from 4.26×10^{-5} to 0.84×10^{-5} s^{-1} as the light source power was reduced from 1011 to 209 W m^{-2} by adjusting the distance of the reaction vessel from the 250 W Hg lamp (Fig. S13b†). A linear plot for light intensity *vs.* k ($R^2 = 0.98$) was obtained (Fig. 8b), indicating the light intensity-dependent nature of the reaction kinetics. The reaction was performed at various temperatures to estimate the apparent activation energy (E_a) (Fig. S13c†).[88] Although the reaction occurred at ambient temperature, the temperature range was extended from 298–318 K to calculate E_a. An elevation in temperature brought about a rise in the reaction rate and k value (Fig. 8c). The Arrhenius equation was employed to determine the E_a value, which was ascertained to be 31.09 kJ mol^{-1} (Fig. 8d). Photogenerated electrons and holes are the main driving forces of the reaction. The rate is affected by the number of charge carriers generated. Nonetheless, the oxidation rate increased as temperature rose under a constant light intensity. Notably, without light, the reaction did not occur in the temperature range of 298–318 K or even at higher temperatures (333 K); the catalyst remained inactive without light.

Experiments were conducted to investigate the photocatalytic oxidation of PS using the exfoliated F-g-C_3N_4 catalyst in different atmospheres. The results revealed that the presence of O_2 was crucial for the reaction (Fig. S14a†). In Ar atmospheres, the reaction activity was minimal, with only 1.3% PS conversion, due to the low quantity of dissolved oxygen (Fig. S14a†). Conversely, the catalyst was more effective in the air, achieving 34.4% conversion with AP as the primary product. To comprehend the reaction mechanism, multiple control experiments were performed. The most active photocatalyst (F-g-C_3N_4) was used in the photocatalytic reaction with TEMPO as a radical scavenger, which led to a significant reduction in catalytic activity (Fig. S14b†). It suggests that various species (electrons, holes, superoxide, and hydroxide radicals) were responsible for the light-assisted reforming of PS. The formation of such species over g-C_3N_4 has been well documented in the literature.

An electron scavenging experiment was performed to examine the importance of photogenerated electrons in light-assisted PS oxidation. CCl_4 and formic acid were used as scavengers, and the photocatalytic activity declined to 39.3% with CCl_4 and 40.9% with formic acid (Fig. S14c†). In both cases, AP emerged as the major product, with selectivity values of 90.2% and 91.1% in CCl_4 and formic acid, respectively. The photogenerated electrons have the potential to convert molecular oxygen into superoxide radicals, which was verified using the NBT test.[89] Photogenerated superoxide radicals decreased NBT concentration, as NBT experienced superoxide-assisted reduction to form diformazan, a blue-colored insoluble precipitate (Fig. S15a†).[90] All the catalysts, *i.e.*, g-C_3N_4 and exfoliated C-g-C_3N_4, T-g-C_3N_4, F-g-C_3N_4, could generate superoxide from oxygen. The F-g-C_3N_4 catalyst was the most effective at generating superoxide radicals, as evidenced by the significant absorption quenching. Furthermore, to validation of superoxide as an intermediate, superoxide trapping was performed using hydroquinone (HQ) and benzoquinone (BQ). The reac-

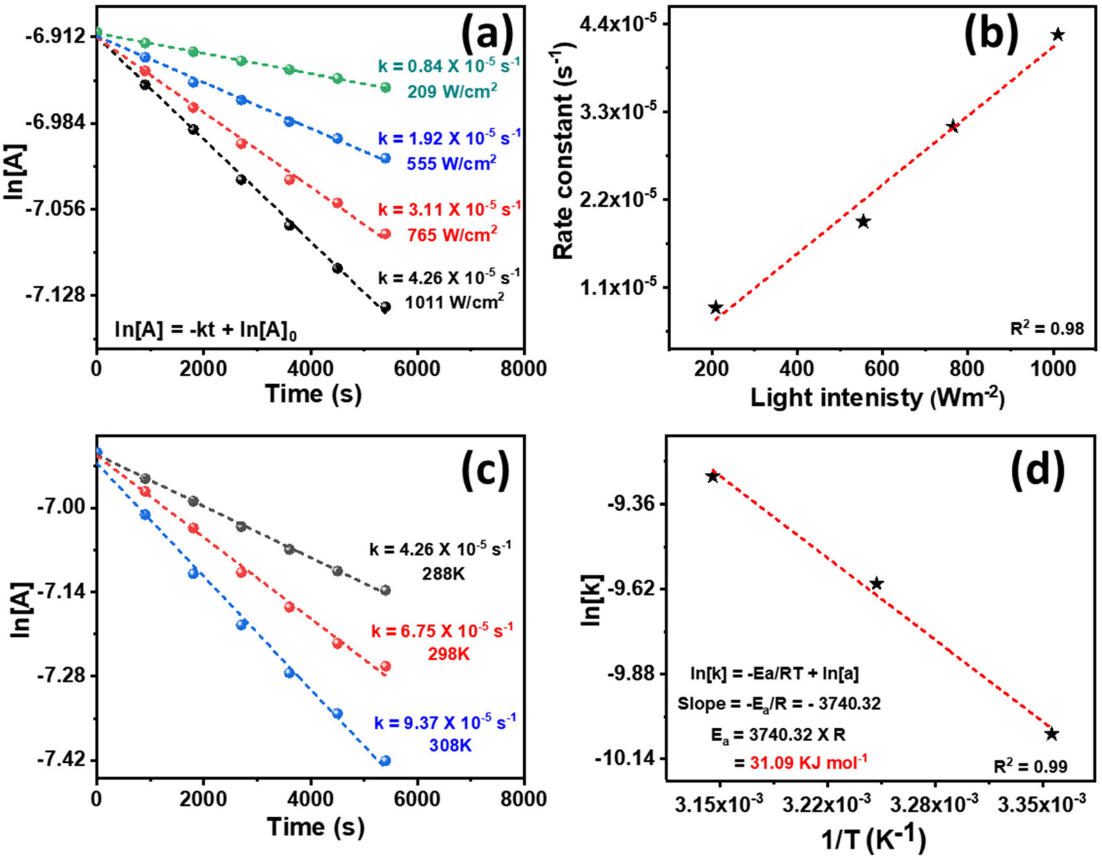

Fig. 8 (a) Graphs illustrating the kinetics of a reaction at different light intensities, (b) k is plotted against light intensity at RT, showing their interdependence, (c) graphs depicting the kinetics of a reaction at different temperatures (298 K, 308 K, and 318 K), and (d) a plot of the ln k *vs.* (1/T) to calculate E_a value.

tion conversion reduced to 59.8% in HQ and 55.3% in BQ; in both cases, AP was the major product (Fig. S14d†).

Light irradiation on photocatalysts generates electrons and holes, with the holes capable of participating in the reaction. To examine the role of holes, hole scavengers such as triethanolamine (TEA) and ethylenediaminetetraacetic acid (EDTA) were employed. The PS conversion was 23.9% in TEA and 27.1% in EDTA, exhibiting high AP selectivity (94.4% and 93.6%, respectively) (Fig. S14e†). The noteworthy decline in activity due to hole scavengers strongly suggests the pivotal role played by holes in the reaction. Additionally, the formation of OH radicals during photocatalytic oxidation was probed using fluorescence quenching experiments with terephthalic acid (THA) on g-C_3N_4 and exfoliated catalysts C-g-C_3N_4, T-g-C_3N_4, and F-g-C_3N_4 (Fig. S15b†).[91] The OH radicals were detected in all cases, with F-g-C_3N_4 showing higher activity and producing more OH radicals. To further investigate the role of OH radicals, scavenging experiments were conducted using *tert*-butyl alcohol (TBA) and methanol (MeOH) as OH radical trappers. The PS conversion reduced to 34.9% in TBA and 33.1% in MeOH (Fig. S14f†), indicating that OH radical quenching effectively reduced the photocatalytic activity. Notably, the E_{VB} of the photocatalyst catalysts is incapable of directly generating OH radicals ([E^θ ($OH^-/{}^\bullet OH$) = 2.40 eV] *vs.* NHE, pH 7),[92] and thus, the catalysts cause it indirectly by degrading the *in situ* generated H_2O_2. The formation of H_2O_2 was verified through the iodometric test (Fig. S15c†), which is engendered from superoxide ions (discussed later).[38,39]

Drawing upon the catalytic activity test, control experiments, scavenging experiments, and physicochemical characterization, a mechanism for the photocatalytic oxidation is proposed (Fig. 9). Initially, PS was adsorbed onto the catalyst surface, followed by light-induced charge separation, resulting in the creation of electron–hole pairs.[93] The electrons migrated to the conduction band (CB), while the holes migrated to the valence band (VB).[94] The electron (e^-) was utilized in the formation of superoxide through oxygen molecule ($O_2 + e^- \rightarrow {}^\bullet O_2^-$), generating superoxide radical anion ($O_2^{\bullet -}$), which was validated through the NBT test.[86] Moreover, the photogenerated hole (h^+) attacks the –C–H bond of the PS molecule, withdrawing an electron (e^-) from it, and activating the C–H bond, resulting in the creation of PS radical and a proton (H^+) (PS + $h^+ \rightarrow {}^\bullet PS + H^+$).[87] The proton ($H^+$) reacted with the superoxide

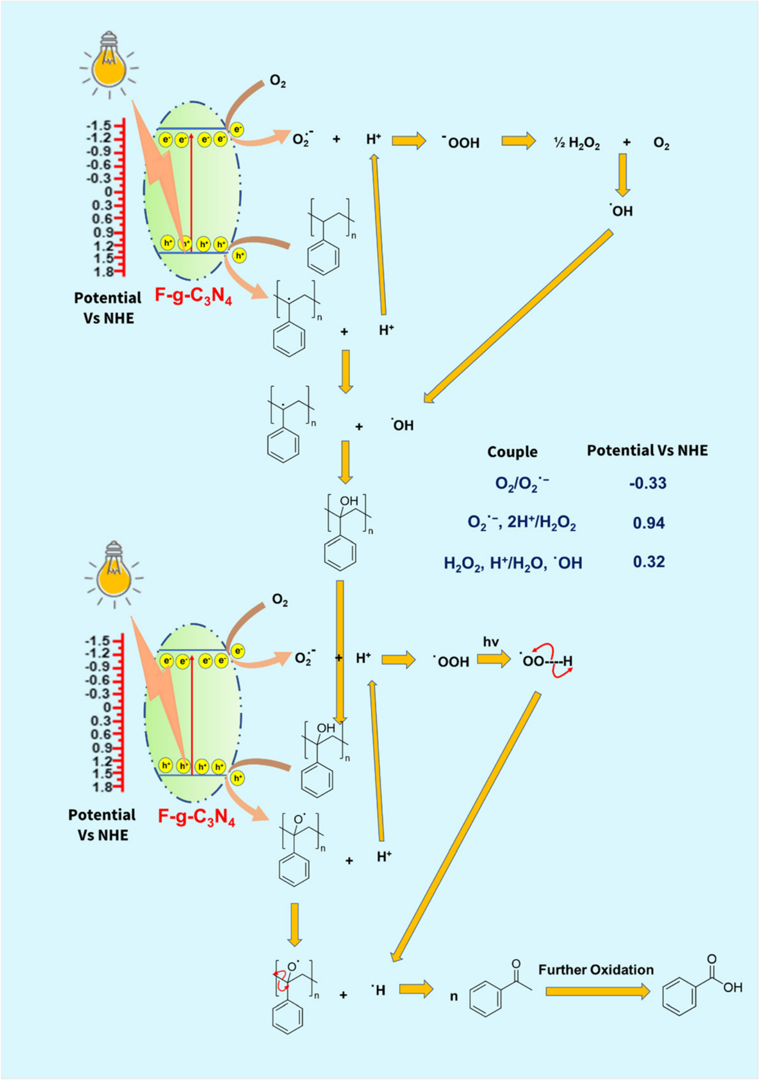

Fig. 9 A plausible mechanism for converting PS into useful chemicals using photocatalysis as a mediator.

radical anion ($O_2^{\bullet-}$) to generate the ($HOO^{\bullet}$) radical ($H^+ + O_2^{\bullet-} \rightarrow HOO^{\bullet}$).[95] Two ($HOO^{\bullet}$) radicals combined to produce H_2O_2 ($2HOO^{\bullet} \rightarrow H_2O_2$) as an intermediate.[39] The formation of H_2O_2 was verified through the iodometric test.[38,39] In the presence of light, H_2O_2 decomposed into ($OH^{\bullet}$) radical ($H_2O_2 \rightarrow OH^{\bullet} + OH^-$), verified by control experiments and the THA test.[95,96] The radical ($OH^{\bullet}$) reacted with the PS radical, forming an intermediate ($^{\bullet}PS + OH^{\bullet} \rightarrow PS\text{–}OH$), which obtained a hole from the VB of the photocatalyst, activating the –OH bond of the intermediate ($PS\text{–}OH + h^+ \rightarrow PS\text{–}O^{\bullet} + H^+$). The interaction produced the $HOO^{\bullet}$ radical from the superoxide and proton. The homolytic cleavage of the C–C bond with $H^{\bullet}$ radical interaction occurred, generating AP, which was subsequently oxidized to BA as a minor product. The time variation study indicated that BA was initially undetectable and formed through the oxidation of AP (Fig. S16†). It was substantiated by a control reaction with AP, which demonstrated that 10% of AP was transformed into BA after 4 h of reaction time (reaction conditions – AP 0.1 m mol, O_2 1 bar, 250 W Hg lamp, and solvent 4 ml).

To ensure the stability of F-g-C_3N_4, a study on catalyst recyclability was conducted. The results indicated that the catalyst maintained its photocatalytic activity without significant degradation for five consecutive cycles (Fig. S17a†). SEM and XRD analysis also showed that the catalyst structure remained unchanged after five cycles (Fig. S17b and c†). Analysis of the DRUV-vis spectra suggested that the spent catalyst had optical properties similar to those of the fresh catalyst (Fig. S17d†). The on–off photocurrent study showed that the recycled photocatalyst responded similarly to the fresh catalyst, exhibiting stable transient photocurrent in each cycle (Fig. S17e†). These results demonstrate that the catalyst was stable and recyclable, and it exhibited exceptional performance and selectivity for PS oxidation under mild conditions.

Conclusions

In summary, this study has successfully demonstrated the efficacious use of photocatalytic techniques in reforming PS into AP and BA. The process involved the oxidation of the C–H, thereby generating functional organic raw materials from plastic waste. The study revealed the capacity of the process to deconstruct addition polymers, consequently generating a valuable product. The synthesis of a flow-mediated exfoliated catalyst, F-g-C_3N_4, was achieved using a tube furnace, and the catalyst manifested impressive properties such as efficient charge separation and photostability and higher transient photocurrent response. The BET analysis indicated a marked augmentation in the surface area after a flow-mediated exfoliation, while the doping of oxygen during the process caused a red shift in the UV-visible spectra, which narrowed the band gap of the material. The F-g-C_3N_4 catalyst proved the most efficient for photocatalytic PS, achieving a conversion rate of ∼63% and ∼86% AP selectivity within 8 h, utilizing a high-pressure Hg lamp. Similarly, under sunlight, the F-g-C_3N_4 catalyst achieved a PS conversion rate of ∼73% and ∼81% benzaldehyde selectivity within 8 h. Furthermore, a solvent study was conducted to eliminate the cumbersome handling of benzene from the protocol, with a sustainable solvent system comprising ethyl acetate : acetonitrile. The reaction rate depended on the light intensity, and the activation energy was calculated to be 31 kJ mol^{-1}. Overall, the study presents a compelling prospect for the plastic recycling industry to convert plastic waste into valuable chemicals while tackling the severe environmental challenge of plastic pollution. The technique's mild conditions, low-cost catalyst, and efficiency make it a powerful strategy for upcycling plastic waste into valuable chemicals.

Author contributions

The work was planned by R. S. and R. G. Experiment work was conducted, and all data were collected by R. G. TEM investigation was performed by R. B. The manuscript was co-written by R. G. and R. S.

Conflicts of interest

There are no conflicts to declare.

Acknowledgements

R. G. expresses gratefulness to CSIR, New Delhi, (09/1005 (0031)/2020-EMR-I) for the fellowship. We are grateful to Central research facility IIT Ropar and SAIF IIT Bombay for the TCPCS analysis.

References

1 X. Li, J. Wang, T. Zhang, S. Yang, M. Sun, X. Qian, T. Wang and Y. Zhao, *Chem. Eng. Sci.*, 2023, 118729.
2 K. Zheng, Y. Wu, Z. Hu, S. Wang, X. Jiao, J. Zhu, Y. Sun and Y. Xie, *Chem. Soc. Rev.*, 2023, **52**, 8–29.
3 S. Thakur, A. Verma, B. Sharma, J. Chaudhary, S. Tamulevicius and V. K. Thakur, *Curr. Opin. Green Sustainable Chem.*, 2018, **13**, 32–38.
4 N. Chaukura, W. Gwenzi, T. Bunhu, D. T. Ruziwa and I. Pumure, *Resour., Conserv. Recycl.*, 2016, **107**, 157–165.
5 C. Marquez, C. Martin, N. Linares and D. De Vos, *Mater. Horiz.*, 2023, **10**, 1625–1640.
6 G. E. De-la-Torre, D. C. Dioses-Salinas, C. I. Pizarro-Ortega and M. Saldaña-Serrano, *Mar. Pollut. Bull.*, 2020, **161**, 111729.
7 A. Turner, *Environ. Sci. Technol.*, 2020, **54**, 10411–10420.
8 B. T. Ho, T. K. Roberts and S. Lucas, *Crit. Rev. Biotechnol.*, 2018, **38**, 308–320.
9 A. Guyot, *Polym. Degrad. Stab.*, 1986, **15**, 219–235.
10 A. V. Prasad and R. P. Singh, *J. Macromol. Sci., Part C: Polym. Rev.*, 1997, **37**, 581–598.
11 A. J. Shah and M. R. Jan, *J. Anal. Appl. Pyrolysis*, 2014, **109**, 196–204.
12 S. Chu, B. Zhang, X. Zhao, H. S. Soo, F. Wang, R. Xiao and H. Zhang, *Adv. Energy Mater.*, 2022, **12**, 2200435.
13 A. Chen, M.-Q. Yang, S. Wang and Q. Qian, *Front. Nanotechnol.*, 2021, **3**, 723120.
14 S. Aldagari, S. F. Kabir, A. Lamanna and E. H. Fini, *Resour., Conserv. Recycl.*, 2022, **183**, 106353.
15 A. A. Shah, F. Hasan, A. Hameed and S. Ahmed, *Biotechnol. Adv.*, 2008, **26**, 246–265.
16 Q. Y. Lee and H. Li, *Micromachines*, 2021, **12**, 907.
17 I. Nabi, A.-U.-R. Bacha, F. Ahmad and L. Zhang, *J. Environ. Chem. Eng.*, 2021, **9**, 105964.
18 J. B. Williamson, S. E. Lewis, R. R. Johnson, I. M. Manning and F. A. Leibfarth, *Angew. Chem., Int. Ed.*, 2019, **58**, 8654–8668.
19 H. Zhou, Y. Wang, Y. Ren, Z. Li, X. Kong, M. Shao and H. Duan, *ACS Catal.*, 2022, **12**, 9307–9324.
20 Z. Huang, M. Shanmugam, Z. Liu, A. Brookfield, E. L. Bennett, R. Guan, D. E. V. Herrera, J. A. Lopez-Sanchez, A. G. Slater, E. J. L. McInnes, X. Qi and J. Xiao, *J. Am. Chem. Soc.*, 2022, **144**, 6532–6542.
21 J. Fu, J. Yu, C. Jiang and B. Cheng, *Adv. Energy Mater.*, 2018, **8**, 1701503.
22 Q. Zhu, Z. Xu, B. Qiu, M. Xing and J. Zhang, *Small*, 2021, **17**, 2101070.
23 S. Samanta and R. Srivastava, *Mater. Adv.*, 2020, **1**, 1506–1545.
24 J. Wen, J. Xie, X. Chen and X. Li, *Appl. Surf. Sci.*, 2017, **391**, 72–123.
25 Y. Li, X. Li, H. Zhang, J. Fan and Q. Xiang, *J. Mater. Sci. Technol.*, 2020, **56**, 69–88.
26 S. Ye, R. Wang, M.-Z. Wu and Y.-P. Yuan, *Appl. Surf. Sci.*, 2015, **358**, 15–27.

27 F. He, Z. Wang, Y. Li, S. Peng and B. Liu, *Appl. Catal., B*, 2020, **269**, 118828.

28 Z. Zhao, Y. Sun and F. Dong, *Nanoscale*, 2015, **7**, 15–37.

29 J. Zhu, P. Xiao, H. Li and S. A. C. Carabineiro, *ACS Appl. Mater. Interfaces*, 2014, **6**, 16449–16465.

30 L. Cheng, H. Zhang, X. Li, J. Fan and Q. Xiang, *Small*, 2021, **17**, 2005231.

31 J. Ma, D. Jin, Y. Li, D. Xiao, G. Jiao, Q. Liu, Y. Guo, L. Xiao, X. Chen, X. Li, J. Zhou and R. Sun, *Appl. Catal., B*, 2021, **283**, 119520.

32 X. Yang, J. Ma, S. Sun, Z. Liu and R. Sun, *Green Chem.*, 2022, **24**, 2104–2113.

33 V. Raji, M. Chakraborty and P. A. Parikh, *Ind. Eng. Chem. Res.*, 2012, **51**, 5691–5698.

34 S. Mishra, S. W. Sangma, R. Bal and R. K. Dey, *New J. Chem.*, 2021, **45**, 13070–13079.

35 B. Gutmann, P. Elsner, D. Roberge and C. O. Kappe, *ACS Catal.*, 2013, **3**, 2669–2676.

36 X. Guan, C. Duan, H. Wang, B. Lu, J. Zhao and Q. Cai, *New J. Chem.*, 2021, **45**, 18192–18201.

37 T. Li, A. Vijeta, C. Casadevall, A. S. Gentleman, T. Euser and E. Reisner, *ACS Catal.*, 2022, **12**, 8155–8163.

38 R. Ghalta and R. Srivastava, *Sustainable Energy Fuels*, 2023, **7**, 1707–1723.

39 R. Ghalta and R. Srivastava, *Catal. Sci. Technol.*, 2023, **13**, 1541–1557.

40 S. S. Wong, M. J. Hülsey, H. An and N. Yan, *Catal. Sci. Technol.*, 2022, **12**, 5217–5228.

41 L. Ye, J. Liu, Z. Jiang, T. Peng and L. Zan, *Appl. Catal., B*, 2013, **142–143**, 1–7.

42 J. Liu, T. Zhang, Z. Wang, G. Dawson and W. Chen, *J. Mater. Chem.*, 2011, **21**, 14398.

43 I. Papailias, N. Todorova, T. Giannakopoulou, N. Ioannidis, N. Boukos, C. P. Athanasekou, D. Dimotikali and C. Trapalis, *Appl. Catal., B*, 2018, **239**, 16–26.

44 S. Challagulla, S. Payra, C. Chakraborty and S. Roy, *Phys. Chem. Chem. Phys.*, 2019, **21**, 3174–3183.

45 P. Niu, L. Zhang, G. Liu and H.-M. Cheng, *Adv. Funct. Mater.*, 2012, **22**, 4763–4770.

46 J. Fu, B. Zhu, C. Jiang, B. Cheng, W. You and J. Yu, *Small*, 2017, **13**, 1603938.

47 J. Sun, J. Zhang, M. Zhang, M. Antonietti, X. Fu and X. Wang, *Nat. Commun.*, 2012, **3**, 1139.

48 J. Xu, L. Zhang, R. Shi and Y. Zhu, *J. Mater. Chem. A*, 2013, **1**, 14766.

49 X. Yue, S. Yi, R. Wang, Z. Zhang and S. Qiu, *Sci. Rep.*, 2016, **6**, 22268.

50 H.-B. Fang, Y. Luo, Y.-Z. Zheng, W. Ma and X. Tao, *Ind. Eng. Chem. Res.*, 2016, **55**, 4506–4514.

51 M. Preeyanghaa, V. Vinesh, P. Sabarikirishwaran, A. Rajkamal, M. Ashokkumar and B. Neppolian, *Carbon*, 2022, **192**, 405–417.

52 X. Yuan, C. Zhou, Y. Jin, Q. Jing, Y. Yang, X. Shen, Q. Tang, Y. Mu and A.-K. Du, *J. Colloid Interface Sci.*, 2016, **468**, 211–219.

53 Z.-F. Huang, J. Song, L. Pan, Z. Wang, X. Zhang, J.-J. Zou, W. Mi, X. Zhang and L. Wang, *Nano Energy*, 2015, **12**, 646–656.

54 J. Li, B. Shen, Z. Hong, B. Lin, B. Gao and Y. Chen, *Chem. Commun.*, 2012, **48**, 12017.

55 Q. Liang, Z. Li, X. Yu, Z.-H. Huang, F. Kang and Q.-H. Yang, *Adv. Mater.*, 2015, **27**, 4634–4639.

56 S. Yang, Y. Gong, J. Zhang, L. Zhan, L. Ma, Z. Fang, R. Vajtai, X. Wang and P. M. Ajayan, *Adv. Mater.*, 2013, **25**, 2452–2456.

57 P. Makuła, M. Pacia and W. Macyk, *J. Phys. Chem. Lett.*, 2018, **9**, 6814–6817.

58 B. D. Viezbicke, S. Patel, B. E. Davis and D. P. Birnie, *Phys. Status Solidi*, 2015, **252**, 1700–1710.

59 H. Razavi-Khosroshahi, K. Edalati, J. Wu, Y. Nakashima, M. Arita, Y. Ikoma, M. Sadakiyo, Y. Inagaki, A. Staykov, M. Yamauchi, Z. Horita and M. Fuji, *J. Mater. Chem. A*, 2017, **5**, 20298–20303.

60 Q. Guo, Y. Zhang, J. Qiu and G. Dong, *J. Mater. Chem. C*, 2016, **4**, 6839–6847.

61 A. O. Oluwole, P. Khoza and O. S. Olatunji, *ChemistrySelect*, 2022, **7**, 202203601.

62 S. Lie, J. M. R. Tan, W. Li, S. W. Leow, Y. F. Tay, D. M. Bishop, O. Gunawan and L. H. Wong, *J. Mater. Chem. A*, 2018, **6**, 1540–1550.

63 D. A. Tran, C. T. N. Pham, T. N. Ngoc, H. N. Phi, Q. T. H. Ta, D. H. Truong, V. T. Nguyen, H. H. Luc, L. T. Nguyen, N. N. Dao, S. J. Kim and V. Vo, *J. Phys. Chem. Solids*, 2021, **151**, 109900.

64 M. V. Dozzi, C. D'Andrea, B. Ohtani, G. Valentini and E. Selli, *J. Phys. Chem. C*, 2013, **117**, 25586–25595.

65 S. P. Pattnaik, A. Behera, S. Martha, R. Acharya and K. Parida, *J. Mater. Sci.*, 2019, **54**, 5726–5742.

66 X. Hu, Q. Ma, X. Wang, Y. Yang, N. Liu, C. Zhang, N. Kawazoe, G. Chen and Y. Yang, *J. Catal.*, 2020, **387**, 28–38.

67 B. Roose, S. Pathak and U. Steiner, *Chem. Soc. Rev.*, 2015, **44**, 8326–8349.

68 L. Wu, Y. Zhang, X. Li and C. Cen, *Phys. Chem. Chem. Phys.*, 2014, **16**, 15339.

69 R. Das, S. Sarkar, R. Kumar, S. D. Ramarao, A. Cherevotan, M. Jasil, C. P. Vinod, A. K. Singh and S. C. Peter, *ACS Catal.*, 2022, **12**, 687–697.

70 H. Guo, H.-Y. Niu, C. Liang, C.-G. Niu, D.-W. Huang, L. Zhang, N. Tang, Y. Yang, C.-Y. Feng and G.-M. Zeng, *J. Catal.*, 2019, **370**, 289–303.

71 K. Gelderman, L. Lee and S. W. Donne, *J. Chem. Educ.*, 2007, **84**, 685.

72 R. Ghalta, A. K. Kar and R. Srivastava, *Chem. – Asian J.*, 2021, **16**, 3790–3803.

73 K. Zhang, W. Kim, M. Ma, X. Shi and J. H. Park, *J. Mater. Chem. A*, 2015, **3**, 4803–4810.

74 S. Hoang, S. Guo, N. T. Hahn, A. J. Bard and C. B. Mullins, *Nano Lett.*, 2012, **12**, 26–32.

75 X. Zhao, Y. Fan, W. Zhang, X. Zhang, D. Han, L. Niu and A. Ivaska, *ACS Catal.*, 2020, **10**, 6367–6376.

76 J. Liu, J. Zhang, D. Wang, D. Li, J. Ke, S. Wang, S. Liu, H. Xiao and R. Wang, *ACS Sustainable Chem. Eng.*, 2019, **7**, 12428–12438.

77 R. Pandiyan, N. Delegan, A. Dirany, P. Drogui and M. A. El Khakani, *J. Phys. Chem. C*, 2016, **120**, 631–638.

78 I. Shown, H.-C. Hsu, Y.-C. Chang, C.-H. Lin, P. K. Roy, A. Ganguly, C.-H. Wang, J.-K. Chang, C.-I. Wu, L.-C. Chen and K.-H. Chen, *Nano Lett.*, 2014, **14**, 6097–6103.

79 R. Beranek, *Adv. Phys. Chem.*, 2011, **2011**, 1–20.

80 H. Fei, W. Leng, X. Li, X. Cheng, Y. Xu, J. Zhang and C. Cao, *Environ. Sci. Technol.*, 2011, **45**, 4532–4539.

81 Y.-S. Jun, W. H. Hong, M. Antonietti and A. Thomas, *Adv. Mater.*, 2009, **21**, 4270–4274.

82 S. Juntrapirom, S. Anuchai, O. Thongsook, S. Pornsuwan, P. Meepowpan, P. Thavornyutikarn, S. Phanichphant, D. Tantraviwat and B. Inceesungvorn, *Chem. Eng. J.*, 2020, **394**, 124934.

83 M. Wang, J. Wen, Y. Huang and P. Hu, *ChemSusChem*, 2021, **14**, 5049–5056.

84 S. Oh and E. E. Stache, *J. Am. Chem. Soc.*, 2022, **144**, 5745–5749.

85 Y. Qin, T. Zhang, H. Y. V. Ching, G. S. Raman and S. Das, *Chem*, 2022, **8**, 2472–2484.

86 N. F. Nikitas, E. Skolia, P. L. Gkizis, I. Triandafillidi and C. G. Kokotos, *Green Chem.*, 2023, **25**, 4750–4759.

87 R. Cao, M.-Q. Zhang, C. Hu, D. Xiao, M. Wang and D. Ma, *Nat. Commun.*, 2022, **13**, 4809–4815.

88 H. Goto, *J. Catal.*, 2004, **225**, 223–229.

89 B. Chen, P. Li, S. Zhang, W. Zhang, X. Dong, F. Xi and J. Liu, *J. Colloid Interface Sci.*, 2016, **478**, 263–270.

90 B. Tryba, M. Toyoda, A. W. Morawski, R. Nonaka and M. Inagaki, *Appl. Catal., B*, 2007, **71**, 163–168.

91 X. Wang, X. Zheng, H. Han, Y. Fan, S. Zhang, S. Meng and S. Chen, *J. Solid State Chem.*, 2020, **289**, 121495.

92 L. Xiong and J. Tang, *Adv. Energy Mater.*, 2021, **11**, 2003216.

93 C. Liang, C. Li, Y. Zhu, X. Du, C. Yao, Y. Ma and J. Zhao, *Chem. Eng. J.*, 2023, **455**, 140461.

94 Y. Zhang, W. Schilling and S. Das, *ChemSusChem*, 2019, **12**, 2898–2910.

95 S. Samanta, S. Khilari, D. Pradhan and R. Srivastava, *ACS Sustainable Chem. Eng.*, 2017, **5**, 2562–2577.

96 T. Jedsukontorn, V. Meeyoo, N. Saito and M. Hunsom, *Chem. Eng. J.*, 2015, **281**, 252–264.